A&A, 710, A62 (2026)
https://doi.org/10.1051/0004-6361/202658963

Astronomy & Astrophysics

A theory of transmission spectroscopy of hydrodynamic outflows from planetary atmospheres: Spectral-line saturation and limits on mass-loss constraints

Leonardos Gkouvelis[⋆]

Instituto de Astrofísica de Andalucía (IAA-CSIC), Glorieta de la Astronomía s/n, 18008 Granada, Spain

Received 14 January 2026 / Accepted 8 April 2026

ABSTRACT

Transmission spectroscopy is a key technique in the characterization of exoplanet atmospheres and has been widely applied to planets undergoing hydrodynamic escape. While a robust analytic theory exists for transmission spectra of hydrostatic atmospheres, the corresponding interpretation for escaping atmospheres has so far relied on numerical modeling, despite the growing number of observations of planetary winds. In this work, a theory of transmission spectroscopy in hydrodynamically escaping atmospheres is developed by coupling the standard transmission geometry to a steady-state, spherically symmetric, isothermal outflow. This approach yields closed-form expressions for the chord optical depth and effective transit radius of a planetary wind and allows the optical depth inversion problem to be examined. The analytic solution reveals that transmission spectroscopy of planetary winds naturally separates into two regimes. In an opacity-limited regime, transmission depths retain sensitivity to the atmospheric mass-loss rate, $\dot{M}$. Beyond a critical threshold, however, spectral-line cores become saturated and no longer provide a unique constraint on the escape rate. This transition is marked by a sharp analytic boundary of the form $\sigma(\lambda)\,\dot{M} \leq C_{\rm sat}$, where $\sigma(\lambda)$ is the line absorption cross section and $C_{\rm sat}$ is a constant set by the thermodynamic and geometric properties of the wind. This condition specifies when the inversion between transmission depth and mass-loss rate admits a real solution. Once it is violated, the effective transit radius is no longer controlled by opacity or mass loss, but by the geometric extent of the absorbing wind. These results demonstrate that spectral-line saturation in transmission spectroscopy corresponds to a fundamental loss of invertibility between absorption and atmospheric mass loss, rather than a gradual weakening of sensitivity. The theory provides a physically transparent explanation for why strong transmission line cores, such as the He triplet or Lyα, may lose unique sensitivity to mass-loss rates once they enter the saturation regime, while weaker lines and the wings of strong lines can remain diagnostic when observationally accessible.

Key words. hydrodynamics – radiative transfer – planets and satellites: atmospheres – planets and satellites: dynamical evolution and stability

1. Introduction

One of the key techniques on which exoplanet atmospheric characterization relies is transmission spectroscopy. During a primary transit, a fraction of the stellar radiation passes through the planetary atmosphere, where it is selectively absorbed or scattered depending on wavelength and atmospheric composition. As a result, the effective planetary radius inferred from transit observations varies with wavelength. This wavelength-dependent modulation of the transit depth encodes information about atmospheric composition, structure, and opacity sources (Brown 2001). Currently, transmission spectra are routinely obtained and interpreted for a wide range of exoplanets, from hot Jupiters to smaller and cooler planets, using both space- and ground-based facilities (e.g., Espinoza et al. 2024; Steinrueck et al. 2025).

While transmission theory in a broader context was developed early on in Earth and planetary sciences, its application to the observational geometry of transiting exoplanets was first presented by Seager & Sasselov (2000). That work identified that atmospheric opacity controls the apparent transit radius and provided a qualitative scaling linking opacity, atmospheric scale height, and transit depth. Later, a closed-form analytic solution was derived by Lecavelier Des Etangs et al. (2008), who showed that, under the assumptions of a hydrostatic and isothermal atmosphere, the effective planetary radius scales logarithmically with opacity as $R_{\rm p}(\lambda) \sim H \ln \kappa(\lambda)$, where H is the atmospheric scale height and $\kappa(\lambda)$ is the wavelength-dependent opacity. This logarithmic scaling has served as a canonical result for more than two decades and has provided valuable intuition for the interpretation of transmission spectra. More recently, Gkouvelis (2026) derived a generalized closed-form expression that accounts for pressure-dependent opacity, modifying the classical scaling to $R_{\rm p}(\lambda) \sim \frac{H}{1+n(\lambda)} \ln \kappa_0(\lambda)$, where n is the power-law exponent describing the pressure dependence of the opacity and κ_0 is a reference opacity. All analytic transmission theories of this kind rely on a common set of assumptions; namely, hydrostatic equilibrium, an isothermal atmosphere, and the absence of strong compositional gradients along the transit chord. In addition, well-known degeneracies affect the normalization of hydrostatic transmission spectra, limiting the unique retrieval of absolute atmospheric properties (Benneke & Seager 2012; de Wit & Seager 2013). Together, these results provide a robust theoretical framework for building intuition and interpreting transmission spectra of stable, hydrostatic atmospheres.

Nevertheless, a significant fraction of the known exoplanet population resides in a non-hydrostatic regime, commonly referred to as a planetary wind (Watson et al. 1981;

[⋆] Corresponding author: `gkouvelis@iaa.es`

Owen 2019), whose onset and long-term persistence can strongly influence the volatile inventory, atmospheric evolution, and potential habitability of rocky planets (Gkouvelis et al. 2025). Under conditions of rapid atmospheric escape, the upper atmosphere is no longer in hydrostatic balance but instead undergoes hydrodynamic outflow, continuously losing mass to space. Transmission spectroscopy has been the primary observational tool for studying this process, mainly through targeted spectral lines with large absorption cross sections that probe atmospheric layers where the outflow is established and where it in some cases extends beyond the Roche lobe (e.g., Lyα, He I 1083 nm; Bourrier et al. 2016; Oklopčić & Hirata 2018).

To date, the interpretation of these observations has relied on numerical models of hydrodynamic escape. One recurring result of such studies is that the cores of strong spectral lines rapidly become insensitive to the mass-loss rate, such that they primarily encode the geometric extent of the absorbing atmosphere rather than the magnitude of the mass flux (Allan & Vidotto 2019; Linssen et al. 2022; Dos Santos et al. 2022). Recent work has highlighted that strong transmission lines, particularly Lyα, do not primarily probe atmospheric mass-loss rates but are instead controlled by geometric and ionization constraints set by the outflow and the stellar environment (Owen et al. 2023).

In contrast, information about the hydrodynamic flow is typically carried by the wings of spectral lines, which remain sensitive to the atmospheric column density and velocity structure (Ballabio & Owen 2025; Lampón et al. 2023). This distinction has so far emerged empirically from numerical modeling, rather than from an analytic transmission framework. These results suggest that the information content of wind transmission spectra is not distributed uniformly across a line profile.

In this work, the standard transmission geometry is coupled to an isothermal, spherically symmetric, steady-state hydrodynamic outflow, and a closed-form expression for the effective transit radius of planetary winds is derived. For wavelengths that probe the atmospheric flow, the analytic solution provides a useful approximation to the transmission spectrum and offers a physical insight into its dependence on opacity, temperature, and mass-loss rate. The analytic framework reveals a fundamental limitation of transmission spectroscopy in escaping atmospheres. It is shown that the mapping between transmission depth and atmospheric mass loss exists only over a restricted range of parameters. Beyond a critical threshold, strong spectral lines become saturated in such a way that the inversion between absorption and mass loss is no longer unique. In this regime, the effective transit radius is set primarily by the geometric extent of the absorbing wind rather than by the mass flux itself. This behavior provides a physical explanation for why the cores of strong transmission lines often lose unique sensitivity to mass-loss rates, while diagnostic information about the hydrodynamic flow may be retained in weaker lines and in the wings of strong transitions. The present theory is intended to identify this intrinsic radiative-transfer limitation. In practice, however, the interpretation of individual tracers may also be affected by additional observational and thermochemical degeneracies, such as interstellar absorption, uncertain level populations, and temperature-dependent ionization or excitation structure.

This work is organized as follows. In Sect. 2, the hydrodynamic outflow model is described and analytic expressions for the chord optical depth and effective transit radius in a steady-state planetary wind are derived. In Sect. 3, the properties and domain of validity of the analytic solution are analyzed, and the regimes in which the inversion between transmission depth and mass-loss rate breaks down are identified. In Sect. 4, the analytic predictions are compared to numerical transmission spectra and the physical interpretation of saturated and opacity-limited regimes is discussed. Finally, Sect. 5 summarizes the main results and their implications for the interpretation of transmission observations of escaping exoplanet atmospheres.

2. Analytic derivation

2.1. Physical assumptions

We examine the planetary winds assuming a steady-state, spherically symmetric, and isothermal flow, which has the mathematical formulation of the Parker wind solution for the solar wind (Parker 1958; Lamers & Cassinelli 1999). Combining the momentum equation, the mass conservation, and the isothermal equation of state, the Parker wind equation was obtained:

$$\left(v^2 - c_s^2\right)\frac{1}{v}\frac{dv}{dr} = \frac{2c_s^2}{r} - \frac{GM_p}{r^2}. \tag{1}$$

The sonic radius, r_s, is defined by the condition $v(r_s) = c_s$. Requiring Eq. (1) to be regular at $r = r_s$ gives

$$r_s = \frac{GM_p}{2c_s^2}. \tag{2}$$

The transonic Parker solution can be written in implicit form as

$$\left(\frac{v}{c_s}\right)^2 - \ln\left[\left(\frac{v}{c_s}\right)^2\right] = 4\ln\left(\frac{r}{r_s}\right) + 4\frac{r_s}{r} - 3. \tag{3}$$

Solving for $n(r)$ in the mass conservation equation, we have the density profile in the radial axis:

$$n(r) = n_s\left(\frac{r_s}{r}\right)^2\frac{c_s}{v(r)}. \tag{4}$$

2.2. Transit geometry

I now considered a ray of starlight passing at an impact parameter, b (measured from the planetary center). Along the line-of-sight coordinate, x, the radial coordinate is

$$r^2 = x^2 + b^2, \tag{5}$$

so that the monochromatic chord optical depth at wavelength λ is

$$\tau(b,\lambda) = 2\int_{r=b}^{+\infty}\sigma(\lambda)\,n(r)\,\frac{r}{\sqrt{r^2-b^2}}\,dr. \tag{6}$$

The transmission geometry and the main characteristic radii of the flow are illustrated in Fig. 1. Substituting Eq. (4) into the optical depth gives

$$\tau(b,\lambda) = 2\sigma(\lambda)\,n_s\,c_s\,r_s^2\int_{b}^{+\infty}\frac{dr}{v(r)\,r\,\sqrt{r^2-b^2}}. \tag{7}$$

This is the exact chord optical depth in a Parker wind, expressed in terms of the velocity profile, $v(r)$, and the sonic-point parameters (r_s, n_s).

To retain analytical tractability, the integral was approximated in the subsonic region of the Parker wind. The geometric

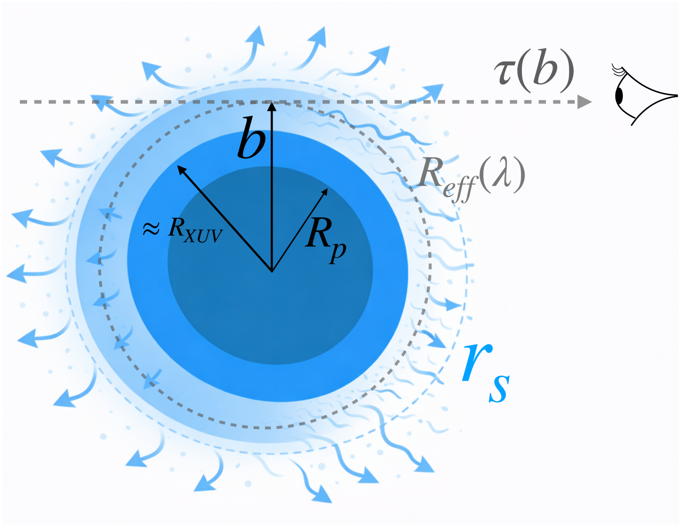

Fig. 1. Geometry of transmission spectroscopy in a planetary wind. A planet of radius R_p is surrounded by a bound hydrostatic atmosphere and an outer hydrodynamically escaping region. Stellar rays intersect the atmosphere along chords of impact parameter b, accumulating a wavelength-dependent slant optical depth, $\tau(b)$, along the line of sight toward the observer. The effective transit radius, $R_{\rm eff}(\lambda)$, is defined by the impact parameter for which $\tau(b)$ reaches the reference value, τ_*. The dashed blue circle marks the sonic radius, r_s, and the approximate location of the XUV photosphere, $R_{\rm XUV}$, is also indicated.

kernel, $1/\sqrt{r^2-b^2}$, peaks strongly near the tangent point $r = b$, so the main contribution to the integral comes from a narrow region around $r \approx b$. This approximation is analogous to the tangent-point treatment commonly adopted in analytic transmission spectroscopy, where the chord optical depth is dominated by a narrow region around the point of closest approach and slowly varying quantities may be evaluated locally (e.g., Lecavelier Des Etangs et al. 2008; de Wit & Seager 2013). In this region, the wind speed varies slowly compared to the geometric factor, and I can approximate $v(r) \approx v(b)$. With this approximation, $v(b)$ is constant with respect to the integration variable, r, so that I can factor it out. Eq. (7) becomes

$$\tau(b,\lambda) \simeq \frac{2\,\sigma(\lambda)\,n_s\,c_s\,r_s^2}{v(b)} \int_b^{+\infty} \frac{dr}{r\,\sqrt{r^2-b^2}}. \tag{8}$$

The remaining integral is purely geometrical and can be evaluated analytically. One finds

$$\int_b^{+\infty} \frac{dr}{r\,\sqrt{r^2-b^2}} = \frac{\pi}{2b}. \tag{9}$$

Inserting Eq. (9) into Eq. (8), I obtain

$$\tau(b,\lambda) \simeq \frac{2\,\sigma(\lambda)\,n_s\,c_s\,r_s^2}{v(b)}\,\frac{\pi}{2b} = \frac{\pi\,\sigma(\lambda)\,n_s\,c_s\,r_s^2}{b\,v(b)}. \tag{10}$$

Equation (10) is a general expression for the chord optical depth in a Parker wind, valid in the approximation that the wind speed is nearly constant over the narrow region around the tangent point $r \approx b$.

2.3. Subsonic approximation

In the subsonic region $r \ll r_s$, the isothermal Parker wind admits a simple asymptotic expression for the velocity (see, e.g., Parker 1958). Starting from the implicit relation (3), one finds that for $v \ll c_s$ the velocity can be written as

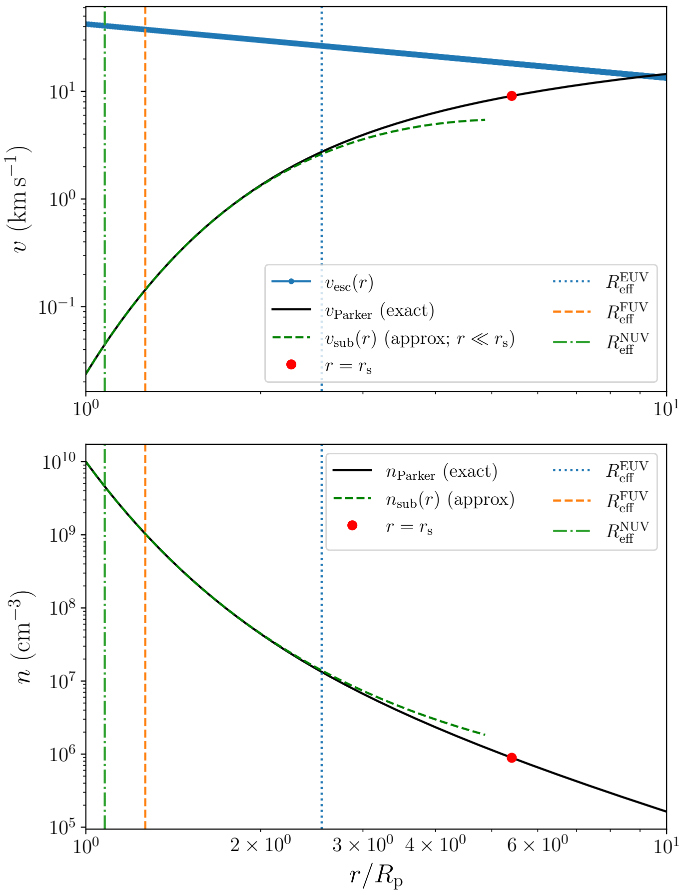

Fig. 2. Radial velocity and density profiles of the Parker wind for the hot Jupiter HD 209458 b. With solid black lines I show the profiles as calculated by the Parker wind formulation, while in dashed green I show the subsonic approximation (see Section 2). For comparison, I overplot the radii where the optical depths of the NUV, FUV, and EUV reach unity, $\tau \approx 1$.

$$v(r) \simeq c_s\,e^{3/2}\left(\frac{r_s}{r}\right)^2 \exp\!\left(-2\frac{r_s}{r}\right), \tag{11}$$

which is valid for radii well below the sonic point, $r \ll r_s$. The numerical prefactor in Eq. (11) depends on the normalization of the transonic solution and is accurate up to a factor of order unity, which does not affect the scaling relations or the qualitative results derived below. A comparison between the exact Parker solution and the subsonic asymptotic approximation is shown in Fig. 2.

Evaluating Eq. (11) at the tangent point $r = b$ and substituting Eq. (11) into Eq. (10) yields

$$\tau(b,\lambda) \simeq \frac{\pi\,\sigma(\lambda)\,n_s\,c_s\,r_s^2}{b\,v(b)} = \pi\,\sigma(\lambda)\,n_s\,e^{-3/2}\,b\,\exp\!\left(2\frac{r_s}{b}\right). \tag{12}$$

For later convenience, a wavelength-dependent prefactor is defined,

$$A(\lambda) \equiv \pi\,\sigma(\lambda)\,n_s\,e^{-3/2}, \tag{13}$$

so that Eq. (12) can be written compactly as

$$\tau(b,\lambda) \simeq A(\lambda)\,b\,\exp\!\left(2\frac{r_s}{b}\right), \qquad (b \ll r_s). \tag{14}$$

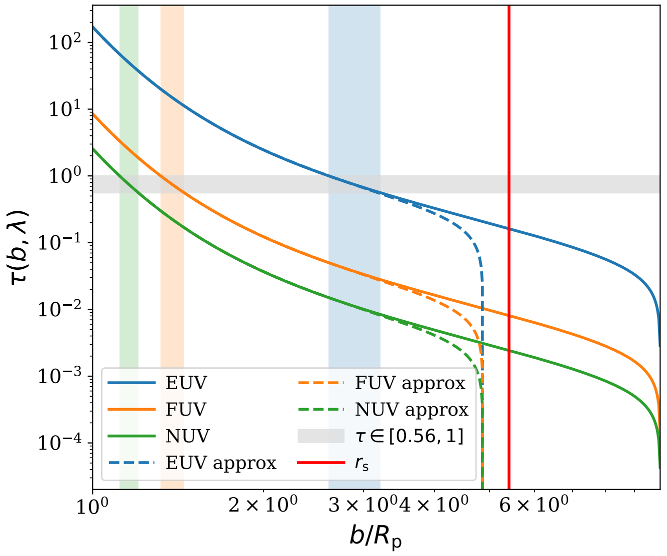

Fig. 3. Optical depth as a function of planet radius for EUV, FUV, and NUV wavelength bands as well as approximations for the same bands overplotted. With shaded stripes I show the range $\tau = 0.56$–1 expressed in terms of the corresponding planet radii for the ultraviolet bands shown.

An example of the resulting chord optical depth profiles for different ultraviolet bands is shown in Fig. 3.

The sonic density is then related to the mass-loss rate. With my assumptions the mass loss rate is written as

$$\dot{M} = 4\pi r^2 \rho(r)\, v(r). \tag{15}$$

Solving for n_s and substituting the resulting expression into Eq. (13), the prefactor $A(\lambda)$ can be written directly in terms of the mass-loss rate:

$$A(\lambda) = \pi\,\sigma(\lambda)\,e^{-3/2}\,\frac{\dot{M}}{4\pi\mu m_p c_s r_s^2} = \frac{\sigma(\lambda)\,\dot{M}}{4\,e^{3/2}\,\mu m_p c_s r_s^2}. \tag{16}$$

2.4. Effective transit radius and Lambert-W solution

In the standard definition, the effective transit radius, $R_\mathrm{eff}(\lambda)$, is obtained from the total obscured area,

$$R_\mathrm{eff}^2(\lambda) = R_0^2 + 2\int_{R_0}^{+\infty} \left[1 - e^{-\tau(b,\lambda)}\right] b\, db, \tag{17}$$

where R_0 is a reference radius (Lecavelier Des Etangs et al. (2008); Gkouvelis (2026)). When $\tau(b,\lambda)$ is a steep function of b, the transmission can be approximated by a sharp transition in opacity. This step-function approximation is standard in transmission theory when the chord optical depth varies rapidly with impact parameter (e.g., Lecavelier Des Etangs et al. 2008; Brown 2001). In this regime it is a good approximation to treat the transmission as a sharp transition at an impact parameter, $b_*(\lambda)$, where the chord optical depth reaches a reference value, $\tau_* \sim O(1)$ (common choices are $\tau_* = 1$ or $\tau_* \simeq 0.56$ (e.g., Lecavelier Des Etangs et al. 2008)). To leading order in this step-function approximation, the effective radius is $R_\mathrm{eff}(\lambda) \approx b_*(\lambda)$, where b_* is defined implicitly by $\tau(b_*,\lambda) = \tau_*$. This steep-$\tau$ approximation provides a closed analytic solution that is valid when the transition between optically thin and optically thick regions occurs over a narrow range of impact parameters. It therefore defines a local inversion between transmission depth and mass-loss rate in the regime in which the effective transit radius can be associated with a characteristic optical-depth surface. The physical interpretation of the resulting saturation boundary in the case of more gradually varying $\tau(b)$ is discussed in Sect. 4.2.

Combining this condition with the subsonic Parker expression (Eq. (14)), I obtain

$$\tau_* = A(\lambda)\, b_*\, \exp\!\left(2\frac{r_s}{b_*}\right), \tag{18}$$

or equivalently

$$D(\lambda) \equiv \frac{\tau_*}{A(\lambda)} = b_*\, \exp\!\left(2\frac{r_s}{b_*}\right), \tag{19}$$

where $D(\lambda)$ has dimensions of length. Finally, I can solve for b_* in closed form using the Lambert-W function (Corless et al. 1996).

I define $y \equiv -2r_s/b_*$, so that $b_* = -2r_s/y$. Substituting into Eq. (19) gives $D = (-2r_s/y)e^{-y}$, and rearranging yields

$$y\,e^{y} = -\frac{2r_s}{D(\lambda)}. \tag{20}$$

By definition of the Lambert-W function, this implies that

$$y = W\!\left(-\frac{2r_s}{D(\lambda)}\right). \tag{21}$$

Using $b_* = -2r_s/y$, I obtain

$$b_*(\lambda) = -\frac{2r_s}{W(-2r_s/D(\lambda))}. \tag{22}$$

To leading order in the step-function approximation, the effective transit radius is

$$R_\mathrm{eff}(\lambda) \approx b_*(\lambda) = -\frac{2r_s}{W(-2r_s/D(\lambda))}. \tag{23}$$

Using $D(\lambda) = \tau_*/A(\lambda)$ and the definition of $A(\lambda)$ (Eq. (16)), I obtain

$$R_\mathrm{eff}(\lambda) \approx -\frac{2r_s}{W\!\left[-\dfrac{\sigma(\lambda)\,\dot{M}}{2\,e^{3/2}\,\tau_*\,\mu m_p c_s r_s}\right]}. \tag{24}$$

Equation (24) is a closed-form expression for the effective transit radius of a steady state isothermal flow in terms of the sonic radius, r_s, sound speed, c_s, mass-loss rate, $\dot{M}$, mean molecular weight, μ, and wavelength-dependent cross section, $\sigma(\lambda)$. The Lambert-W solution branch determines the physically relevant solution and is discussed in Section 3.1.

3. Validity, branches, and saturation boundary

The effective transit radius is obtained by inverting the condition $\tau(b,\lambda) = \tau_*$. This inversion is mathematically equivalent to solving a Lambert-W equation. Whether this equation admits a real solution determines whether transmission spectroscopy provides a unique mapping between absorption depth and atmospheric mass loss. I thus demonstrate that this mapping exists only below a sharp threshold in $\sigma(\lambda)\dot{M}$, and derive this threshold explicitly.

3.1. Lambert-w branches and the physical solution

The regime of validity of Eq. (24) is now discussed, along with the identification of the Lambert-W branch that yields a physically meaningful solution in the subsonic region. The Lambert-W function is defined implicitly by $W(z)\,e^{W(z)} = z$. For real arguments, z, the function has a single real branch, $W_0(z)$, for $z \geq 0$, two real branches, $W_0(z)$ and $W_{-1}(z)$, for $-1/e \leq z < 0$, and only complex values for $z < -1/e$ (Corless et al. 1996). On the interval $-1/e \leq z < 0$, the principal branch satisfies $-1 \leq W_0(z) < 0$, while the lower branch satisfies $W_{-1}(z) \leq -1$.

For this application, it is convenient to define

$$z(\lambda) \equiv -\frac{\sigma(\lambda)\,\dot{M}}{2\,e^{3/2}\,\tau_*\,\mu m_p c_s r_s}, \tag{25}$$

so that Eq. (24) becomes

$$R_{\rm eff}(\lambda) \approx -\frac{2r_s}{W(z(\lambda))}. \tag{26}$$

Since $\sigma(\lambda) > 0$ and $\dot{M} > 0$, I have $z(\lambda) < 0$ for all wavelengths.

The derivation leading to Eq. (26) assumes that the effective radius lies deep in the subsonic region of the Parker wind, $R_{\rm eff}(\lambda) \ll r_s$. Introducing

$$y \equiv -\frac{2r_s}{R_{\rm eff}}, \tag{27}$$

I have $y = W(z(\lambda))$ and $R_{\rm eff} = -2r_s/y$. The subsonic requirement $R_{\rm eff} \ll r_s$ implies $|y| \gg 2$, i.e., the solution of $y\,e^y = z(\lambda)$ must have a large negative magnitude. On $-1/e \leq z < 0$, the two real branches behave differently:
(i) On the principal branch $W_0(z)$, $-1 \leq W_0(z) < 0$; hence, $|y| \lesssim 1$ and $R_{\rm eff} \gtrsim 2r_s$, which is inconsistent with $R_{\rm eff} \ll r_s$.
(ii) On the lower branch $W_{-1}(z)$, $W_{-1}(z) \leq -1$ and $|W_{-1}(z)| \to \infty$ as $z \to 0^-$, implying that $|y| \gg 1$, and thus that $R_{\rm eff} \ll 2r_s$, which is consistent with the subsonic approximation.

Therefore, within the regime in which the subsonic Parker approximation is valid and $z(\lambda) \in [-1/e, 0)$, the physically relevant solution is obtained by choosing the W_{-1} branch:

$$R_{\rm eff}(\lambda) \approx -\frac{2r_s}{W_{-1}(z(\lambda))}, \qquad -\frac{1}{e} \leq z(\lambda) < 0. \tag{28}$$

3.2. Real versus complex solutions and the onset of saturation

For $z(\lambda) < -1/e$, the Lambert–W function has no real values, and Eq. (26) yields a complex $R_{\rm eff}$ that has no direct geometric interpretation. In practice, a complex solution is best interpreted as a diagnostic that one (or more) assumptions entering the analytic inversion have broken down. In the present context, the most relevant interpretation is that the optical-depth criterion, $\tau(b, \lambda) = \tau_*$, cannot be satisfied at any b within the subsonic regime because the line is saturated: the chord optical depth exceeds τ_* for all grazing chords that remain in the region where the subsonic approximation applies. Equivalently, the real-domain condition $z(\lambda) \geq -1/e$ defines a sharp boundary in $(\sigma, \dot{M})$ space beyond which the analytic inversion ceases to exist as a real-valued mapping.

3.3. A single dimensionless control parameter and a quantitative validity boundary

The analytic expression for the effective transit radius in a Parker wind, Eq. (28), depends on wavelength only through the product of opacity and mass-loss rate. This motivates defining a dimensionless control parameter,

$$\chi(\lambda) \equiv \frac{\sigma(\lambda)\,\dot{M}}{\mu\,m_p\,c_s\,r_s}, \tag{29}$$

such that

$$z(\lambda) = -\frac{\chi(\lambda)}{2e^{3/2}\tau_*}. \tag{30}$$

The analytic solution exists only for real values on the W_{-1} branch, requiring

$$-\frac{1}{e} \leq z(\lambda) < 0, \tag{31}$$

which is equivalent to an upper bound on $\sigma(\lambda)\dot{M}$:

$$\sigma(\lambda)\,\dot{M} \;\leq\; C_{\rm sat}, \tag{32}$$

where $C_{\rm sat} \equiv 2e^{1/2}\tau_*\mu m_p c_s r_s$. This inequality is the quantitative saturation boundary: when it is satisfied, the inversion between absorption and effective transit radius is real-valued and well defined; when it is violated, the corresponding wavelength lies in a saturation-limited regime in which the analytic inversion breaks down. This analytic saturation boundary and the two transmission regimes are illustrated quantitatively in Fig. 6, utilizing HD 209458 b as an example.

3.4. Limitations of the asymptotic expansion

One may formally expand the Lambert-W function for small $|z|$ as

$$W(z) = z - z^2 + \frac{3}{2}z^3 + O(z^4), \tag{33}$$

which yields a simple approximate scaling of $R_{\rm eff}$ with $\sigma(\lambda)$ and n_s. However, the series (33) is an expansion around $z = 0$ on the principal branch, W_0, where $W(z) \to 0$ as $z \to 0$. Because $W_0(z) \in [-1, 0)$ for $z \in [-1/e, 0)$, this would imply that $R_{\rm eff} \gtrsim 2r_s$, i.e., outside the subsonic region where my Parker asymptotics were derived.

By contrast, on the physically relevant branch W_{-1} one has $W_{-1}(z) \to -\infty$ as $z \to 0^-$, and the appropriate asymptotic is logarithmic rather than a power series (e.g., Corless et al. 1996). Consequently, the small-$|z|$ expansion (33) is mathematically correct but not self-consistent for the physical regime of interest ($R_{\rm eff} \ll r_s$). For quantitative work, it is therefore recommended to use Eq. (28) with the W_{-1} branch and check a posteriori that $R_{\rm eff}(\lambda) \ll r_s$ for the parameters of interest.

4. Physical interpretation and synthetic spectra

4.1. Analytic transmission synthetic spectra of planetary winds

Setup and numerical framework. The analytic model for non-hydrostatic atmospheres is now tested by computing synthetic

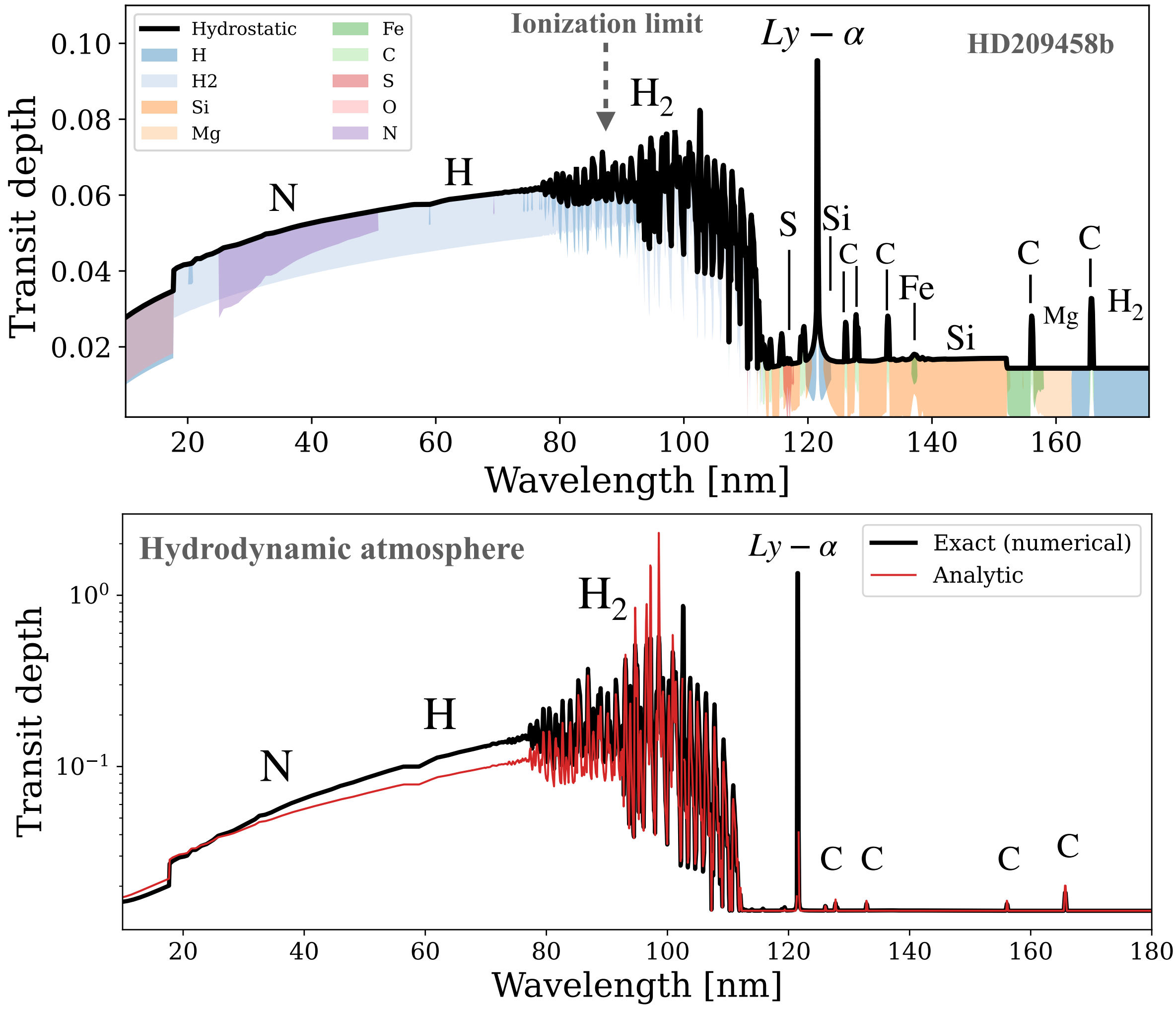

Fig. 4. Up: transmission spectrum of HD 209458 b under the hydrostatic and stable thermosphere hypothetical scenarios. With shaded regions the dominant absorption species at each wavelength are indicated. Bottom: comparison of HD 209458 b hydrodynamic atmosphere's transmission spectrum from numerical integration including line broadening effects from bulk flow and thermal motion, compared to the analytic model derived in Eq. (28).

transmission spectra. To trace the upper atmosphere and thus the hydrodynamic flow, we can focus on wavelength regions with large absorption cross sections. Ultraviolet wavelengths are particularly well suited for this purpose, especially for broadband coverage.

In Fig. 4, synthetic transmission spectra for the hot Jupiter HD 209458 b are presented. They comprise a benchmark system that is well studied observationally and known to undergo hydrodynamic atmospheric escape (Vidal-Madjar et al. 2003, 2004; Murray-Clay et al. 2009). Spectra in the ultraviolet range ($\lambda \approx$ 15–180 nm) were computed for comparison between a hydrostatic (upper panel) and a hydrodynamic Parker-wind scenario (lower panel). The numerical spectra were computed following Appendix A. Planetary and atmospheric parameters were adopted from representative literature values (e.g., Koskinen et al. 2010, 2013). Ultraviolet photoabsorption cross sections were compiled from multiple sources (Heays et al. 2017; Gkouvelis et al. 2018; Chubb et al. 2024; Gkouvelis et al. 2024), and references therein.

Failure of hydrostatic transmission intuition. The hydrostatic calculation (upper panel of Fig. 4) is included only as a baseline that illustrates what ultraviolet opacities would imply under the assumptions of hydrostatic transmission theory. The resulting spectral morphology differs qualitatively from the wind case: once the atmosphere is not in hydrostatic balance, the mapping between opacity, structure, and transit depth is fundamentally altered. This demonstrates that the physical intuition built from analytic transmission theory for hydrostatic atmospheres does not carry over to the planetary-wind regime.

Analytic–numerical comparison and saturation. In the lower panel of Fig. 4, the black curve shows the numerical transmission spectrum obtained by line-by-line integration through the full Parker wind density profile (Eq. (4)). The red curve shows the analytic prediction from Eq. (28). The overall agreement confirms that the analytic solution captures the dominant physics of transmission through a hydrodynamically escaping atmosphere in the regime in which the subsonic and step-function approximations apply, while departures at strongly saturated wavelengths motivate the more general hydrodynamic interpretation discussed in Section 4.2. At several wavelengths, however, the analytic solution does not admit a real-valued Lambert-W solution. A characteristic example is the Lyα line core. In the numerical model, the effective radius reaches very large values, as expected for a strongly saturated resonance line. In contrast,

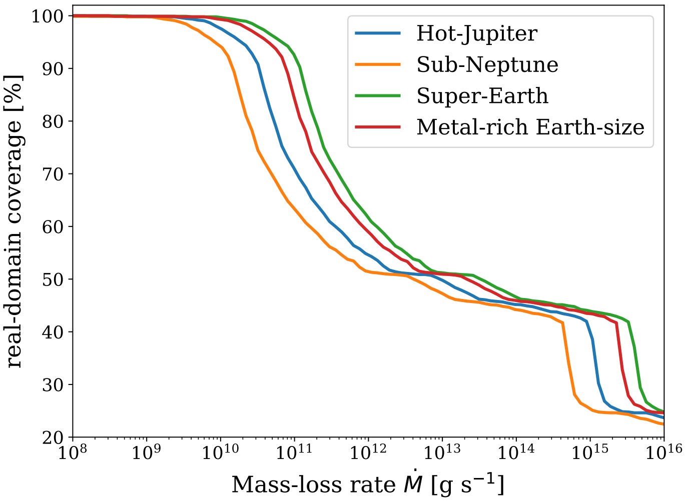

Fig. 5. Analytic coverage as a function of wavelength, defined as the fraction of wavelength points for which the Lambert-W argument satisfies $-1/e \leq z(\lambda) < 0$. This condition ensures a real-valued effective transit radius, and therefore identifies the wavelength range in which the analytic inversion remains valid.

the analytic inversion fails because the real-domain condition in Eq. (28) is violated, i.e., $z(\lambda) < -1/e$. The numerical spectrum remains well defined in this regime: it is the analytic inversion between the optical-depth criterion and the effective radius that breaks down, not the underlying radiative-transfer calculation.

This connects directly to the saturation boundary derived in Sect. 3.3. Wavelengths for which Eq. (32) is satisfied correspond to an opacity-limited regime in which $R_{\rm eff}$ remains sensitive to $\dot{M}$ and other physical parameters. Wavelengths for which the inequality is violated lie in a saturation-limited regime: the optical depth exceeds the adopted threshold along all relevant grazing chords, and the mapping between absorption depth and mass loss is no longer invertible. In this sense, saturation is not merely a gradual reduction in sensitivity, but a sharp loss of invertibility that follows from the analytic structure of the solution.

Expressed in this way, the analytic Parker-wind transmission spectrum highlights that the observable extent of an escaping atmosphere is determined by the interplay between opacity and mass flux, rather than by pressure normalization alone. The sonic radius provides the natural geometric scale controlling the extent of the optically thick region. In Fig. 5 the fraction of wavelengths in the ultraviolet that satisfy the real-domain condition $-1/e \leq z(\lambda) < 0$ are shown, i.e., the fraction of wavelength points where the analytic inversion remains valid, across a range of mass-loss rates.

4.2. Hydrodynamic interpretation of the saturation boundary beyond the steep-τ approximation

The analytic derivation presented in the previous sections provides a closed-form inversion between transmission depth and mass-loss rate under the steep-τ approximation commonly used in analytic transmission theory. The resulting saturation boundary therefore identifies the regime in which this analytic inversion ceases to admit a unique solution. In this section I examine the regime in which the steep-τ approximation fails, and show how the resulting saturation behavior can be interpreted in a more general hydrodynamic context. Even when the optical depth varies gradually with impact parameter (e.g., Ballabio & Owen (2025)), the exact transmission integral naturally separates opacity-limited and saturation-limited regimes.

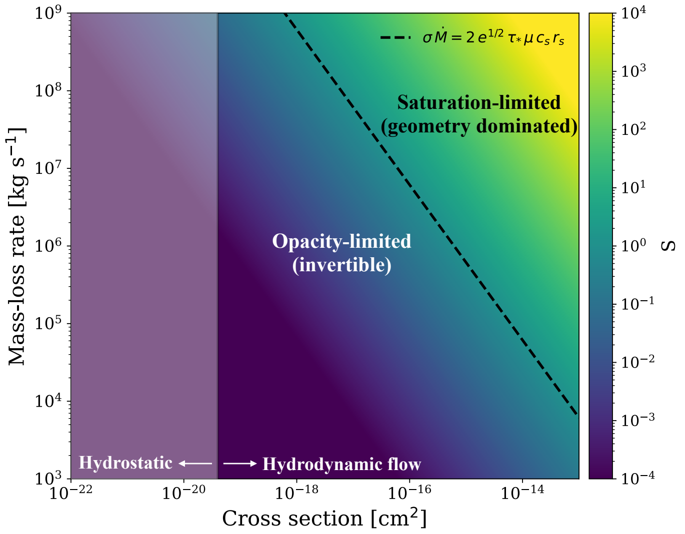

Fig. 6. Regime map for transmission through a hydrodynamic planetary wind, shown in the plane of the absorption cross section, $\sigma(\lambda)$, and mass-loss rate, $\dot{M}$, for HD 209458 b. The color scale represents the dimensionless saturation parameter $S \equiv \sigma(\lambda)\dot{M}/C_{\rm sat}$, where $C_{\rm sat} = 2e^{1/2}\tau_*\mu m_p c_s r_s$. The dashed black curve marks the analytic validity boundary $\sigma(\lambda)\dot{M} = C_{\rm sat}$, separating the opacity-limited regime ($S \ll 1$), in which the transmission depth scales linearly with $\sigma\dot{M}$, from the saturation-limited regime ($S \gg 1$), in which the effective transit radius is set primarily by geometry. The shaded light gray region indicates cross sections of $\sigma \lesssim \sigma_{\rm obs,base} \sim 4 \times 10^{-20}\,{\rm cm}^2$, for which absorption becomes optically thin above the XUV heating base and the observed signal is expected to probe below the wind launch region. This figure illustrates the sharp, quantitative boundary between invertible and non-invertible transmission regimes predicted by the analytic model.

In the analytic inversion derived in the previous section, the transmission integral is dominated by a narrow annulus around b_*. However, the fundamental observable is the exact transmission-area integral given in Equation (17), which does not require the steep-τ assumption. The transmission signal therefore naturally separates two regimes depending on the magnitude of the optical depth.

Opacity-limited regime. If the atmosphere is optically thin over most of the contributing region,

$$\tau(b,\lambda) \ll 1, \tag{34}$$

then $1 - e^{-\tau} \simeq \tau$ and the transmission signal becomes approximately proportional to the optical depth,

$$R_{\rm eff}^2 - R_0^2 \propto \int \tau(b,\lambda)\, b\, db. \tag{35}$$

Since the optical depth scales linearly with the mass-loss rate, $\tau \propto \sigma(\lambda)\dot{M}$, the observable absorption also scales approximately with $\dot{M}$. In this regime the mapping between the transmission depth and the mass-loss rate remains approximately invertible.

Saturation-limited regime. If the inner region of the outflow becomes optically thick,

$$\tau(b,\lambda) \gg 1 \tag{36}$$

for $b < b_{\rm sat}$, the integrand approaches unity, and the contribution from this region becomes purely geometric,

$$\int_{R_0}^{b_{\rm sat}} b\, db = \frac{1}{2}(b_{\rm sat}^2 - R_0^2). \tag{37}$$

Increasing the column density further does not significantly increase the absorption from this region. The transmission signal becomes controlled by the projected size of the saturated region and by the optically thin outer tail of the atmosphere rather than by the total column density. In this regime the mapping between transmission depth and mass-loss rate loses uniqueness.

We can now derive the scaling of the optical depth as a function of the impact parameter, b, in the context of a general hydrodynamic outflow. Starting from the steady wind density profile

$$n(r) = \frac{\dot{M}}{4\pi\mu m_p r^2 v(r)}, \tag{38}$$

and inserting it into the chord optical depth integral, one obtains

$$\tau(b,\lambda) = \sigma(\lambda)\int n(r)\, ds \sim \frac{\sigma(\lambda)\dot{M}}{4\,\mu m_p}\int \frac{ds}{r^2 v(r)}. \tag{39}$$

Approximating the integral near the tangent point, where the geometric kernel peaks (i.e., $r \sim b$) and $v(r) \sim v(b)$, yields the scaling

$$\tau(b,\lambda) \propto \frac{\sigma(\lambda)\dot{M}}{b\, v(b)}. \tag{40}$$

In particular, this step does not assume that the optical depth varies rapidly with impact parameter, but only that the dominant contribution to the integral arises from the vicinity of the tangent point due to geometric projection. This scaling is consistent with the analytic condition derived in Section 3.3, in which the product $\sigma(\lambda)\dot{M}$ acts as the fundamental control parameter determining whether the transmission signal lies in the opacity-limited or saturation-limited regime.

A useful hydrodynamic estimate of the saturation scale can be obtained by defining the impact parameter, $b_{\rm sat}$, at which the optical depth becomes of order unity,

$$\tau(b_{\rm sat},\lambda) \sim 1. \tag{41}$$

Using the scaling above gives

$$b_{\rm sat}(\lambda) \sim \frac{\sigma(\lambda)\dot{M}}{v(b_{\rm sat})}. \tag{42}$$

This relation shows that stronger transitions (larger $\sigma(\lambda)$) and larger mass-loss rates extend the saturated region to larger impact parameters, while faster winds reduce the optical depth and shrink the saturated region. The analytic saturation boundary derived above may therefore be interpreted as identifying the transition where the steep-τ inversion ceases to be valid and the transmission signal becomes dominated by the geometric extent of the optically thick region of the outflow. The hydrodynamic scaling above also clarifies the meaning of the analytic saturation boundary derived in the previous sections. If the onset of saturation is defined by the condition $\tau(b_{\rm sat},\lambda) \sim 1$, then $\tau(b,\lambda) \propto \sigma(\lambda)\dot{M}/[b\, v(b)]$ implies

$$\sigma(\lambda)\dot{M} \sim b_{\rm sat}\, v(b_{\rm sat}). \tag{43}$$

The product $\sigma(\lambda)\dot{M}$ therefore determines how far outward the optically thick region extends along the line of sight. The analytic saturation condition derived earlier may then be interpreted as the local steep-τ realization of this more general hydrodynamic transition: once the saturated region expands to the characteristic transmission radius, the inversion between transit depth and mass-loss rate ceases to be unique.

5. Discussion

5.1. Information content of transmission spectra in planetary winds

The analytic framework developed in this work shows that transmission spectroscopy of hydrodynamically escaping atmospheres is fundamentally governed by the mathematical structure of the optical depth inversion problem. When the argument of the Lambert-W function remains within its real-valued domain, the effective transit radius is a single-valued and monotonic function of the product $\sigma(\lambda)\dot{M}$, and the transmission spectrum is opacity-limited. In this regime, variations in mass-loss rate, temperature, mean molecular weight, or absorber abundance lead to measurable changes in the transit depth, and the analytic solution accurately reproduces numerical radiative-transfer calculations.

Once the real-domain condition is violated, the inversion ceases to exist as a real-valued mapping. This defines a sharp transition to a saturation-limited regime, in which the optical depth along all relevant grazing chords exceeds the reference threshold, τ_*. In this case, further increases in opacity or mass flux do not lead to a unique increase in the effective transit radius. This saturation regime reflects a failure of the analytic inversion, not of radiative transfer itself: fully numerical transmission spectra remain well defined and continuous in this limit. Transmission spectroscopy therefore loses its ability to uniquely constrain the atmospheric column density or the mass-loss rate at those wavelengths.

This behavior provides a natural explanation for the longstanding result from numerical models that the cores of strong resonance lines (e.g., Lyα, Hα) often show weak sensitivity to $\dot{M}$ when they lie in the saturation-limited regime. In the analytic framework presented here, this occurs when the line core lies beyond the saturation boundary, such that the effective transit radius becomes insensitive to further increases in opacity or mass flux.

For the He I 1083 nm triplet, previous studies have shown that the observable absorption is often dominated by optically thin regions of the flow, leading to a stronger dependence on $\dot{M}$ (Ballabio & Owen 2025; Linssen & Oklopčić 2023). More generally, this highlights that different spectral lines probe different regimes of the outflow depending on their opacity and excitation conditions.

From an observational perspective, this implies that transmission spectra should not be interpreted uniformly across wavelength. Instead, spectral regions should be classified according to whether they lie in the opacity-limited or saturation-limited regime. Only the former admit an approximately unique mapping between absorption depth and the underlying escape parameters within the present analytic framework.

5.2. Geometric nature of saturated line cores

In the saturation-limited regime, the Lambert-W solution approaches the branch point and the effective transit radius asymptotically converges to

$$R_{\rm eff} \to 2r_s, \tag{44}$$

where

$$r_s = \frac{GM_p}{2c_s^2} \tag{45}$$

is the sonic radius of the Parker wind. This saturation scale depends only on the planetary gravitational potential and the atmospheric temperature through the sound speed, and is independent of both the absorption cross section and the mass-loss rate. The observable absorption depth in saturated line cores therefore reflects the geometric extent of the optically thick region rather than the atmospheric column density or mass flux.

The existence of the saturation boundary follows from the analytic structure of the optical-depth inversion and therefore arises independently of the specific numerical implementation of radiative transfer. Its precise location depends on the product $\sigma(\lambda)\dot{M}$ and on the global thermodynamic properties of the wind. In real systems, the observable geometric extent may be truncated at smaller radii by ionization fronts, interaction with the stellar wind, or Roche-lobe effects.

This result demonstrates that the weak sensitivity of saturated line cores to $\dot{M}$ is not a numerical artifact or a gradual loss of signal, but a direct consequence of the non-invertibility of the optical-depth condition in an expanding atmosphere. Two planets with a similar temperature and gravity but substantially different mass-loss rates can therefore exhibit nearly identical saturated line cores, provided that both lie beyond the analytic saturation boundary. Consequently, strong transmission lines primarily constrain geometric properties of the upper atmosphere, such as the radial extent of the absorbing species and the termination altitude set by ionization or dissociation processes, whereas quantitative constraints on mass loss must rely on opacity-limited diagnostics.

Finally, it is worth noting that the expressions for the effective transit radius, Eqs. (17), (35), implicitly assume that the optical depth decreases sufficiently rapidly at large impact parameters for the corresponding integrals to converge. However, in a Parker wind the density profile asymptotically approaches a r^{-2} scaling in the supersonic regime, which implies that the chord optical depth does not decrease faster than $1/b^2$. As a result, the integral for the obscured area would formally diverge if extended to infinite radius. In practice, this divergence is avoided because real planetary outflows have a finite spatial extent. The escaping atmosphere is truncated by physical processes such as photoionization, interaction with the stellar wind, or confinement within the Roche lobe, which introduce an effective outer cutoff radius. The observable absorption is therefore dominated by the region where the optical depth transitions through unity, and the scaling relations derived here remain valid, as they are controlled by the inner regions of the flow rather than by the asymptotic behavior at large radii.

5.3. Connection to the escape parameter and hydrostatic structure

The sonic radius provides a physically transparent link between transmission spectroscopy of winds and classical escape theory. Introducing the Jeans escape parameter evaluated at the planetary radius,

$$\lambda_0 \equiv \frac{GM_p\mu}{kTR_p}, \tag{46}$$

one obtains

$$\frac{r_s}{R_p} = \frac{\lambda_0}{2}. \tag{47}$$

The saturation scale $R_{\rm eff} \simeq 2r_s$ therefore corresponds to a fixed fraction of the gravitational binding depth of the atmosphere. This highlights a fundamental difference with hydrostatic transmission spectra, in which the effective radius is anchored to an arbitrary reference pressure level. In planetary winds, by contrast, the observable extent of the atmosphere is controlled by the depth of the gravitational potential well and the thermal state of the gas.

5.4. Interpretation in the energy-limited escape framework

Although the analytic solution is expressed in terms of the mass-loss rate, it is instructive to reinterpret the results under the assumption of approximately energy-limited escape,

$$\dot{M}_{\rm EL} = \frac{\eta\pi R_{\rm XUV}^3 F_{\rm XUV}}{GM_pK}, \tag{48}$$

where η is the heating efficiency, $R_{\rm XUV}$ the effective absorption radius, $F_{\rm XUV}$ the stellar high-energy flux, and K the Roche-lobe correction factor.

Substituting this expression into the dimensionless control parameter $\chi(\lambda)$ yields the scaling

$$\chi(\lambda) \propto \frac{\sigma(\lambda)\,\eta\,F_{\rm XUV}\,R_{\rm XUV}^3\,\sqrt{T}}{(GM_p)^2\,\mu^{3/2}}, \tag{49}$$

up to numerical factors of order unity. This relation shows that, at fixed opacity, the transmission spectrum of a planetary wind is most sensitive to stellar irradiation and planetary mass, and only weakly dependent on temperature, while retaining a stronger dependence on the mean molecular weight through the sound-speed scaling. Within this framework, the analytic saturation boundary can be interpreted as a threshold in stellar forcing beyond which the subsonic region of the outflow becomes optically thick at the wavelengths considered. Strongly irradiated, low-gravity planets are therefore expected to exhibit saturated line cores over wide spectral intervals, whereas higher-gravity or weakly irradiated planets may remain in the opacity-limited regime even for intrinsically strong transitions.

5.5. Implications for observations and retrievals

The analytic results presented here provide a quantitative criterion for assessing the diagnostic power of different spectral tracers of atmospheric escape. Wavelength regions that satisfy the real-domain condition of the Lambert-W solution admit a unique mapping between transmission depth and atmospheric parameters and are therefore suitable for quantitative mass-loss constraints. Regions that violate this condition lose unique sensitivity to the mass-loss rate and primarily probe the geometric extent of the absorbing atmosphere.

This distinction offers practical guidance for observational strategies and retrieval analyses. In particular, weaker transitions and the wings of strong lines are more likely to remain in the opacity-limited regime, where the transmission signal retains a direct sensitivity to the atmospheric column density and mass-loss rate, although weaker transitions may be more challenging to detect observationally due to their smaller absorption depth, particularly for UV diagnostics. Strong lines, on the other hand, are often easier to detect and can provide both line cores and wings, but their cores may enter the saturation regime, in which case the observable absorption depth primarily reflects the geometric extent of the escaping atmosphere rather than the mass flux itself.

In practice, additional factors may further complicate the interpretation of observations. For example, Lyα line cores are frequently obscured by interstellar absorption and the observable signal is typically inferred from the line wings, where interactions with the stellar environment may play an important role (e.g., Owen et al. 2023). Likewise, interpretation of the helium 1083 nm triplet depends on the thermodynamic structure of the outflow, including the temperature, the H/He abundance ratio, and the fraction of helium atoms in the metastable triplet state (e.g., Dos Santos et al. 2022). Such effects introduce additional degeneracies that can affect mass-loss estimates even when the opacity-limited condition is satisfied.

Acknowledgements. The author acknowledges financial support from the Severo Ochoa grant CEX2021-001131-S funded by MCIN/AEI/10.13039/501100011033 and Ministerio de Ciencia e Innovación through the project PID2022-137241NB-C43.

References

Allan, A., & Vidotto, A. A. 2019, MNRAS, 490, 3760
Ballabio, G., & Owen, J. E. 2025, MNRAS, 537, 1305
Benneke, B., & Seager, S. 2012, ApJ, 753, 100
Bourrier, V., Lecavelier des Etangs, A., Ehrenreich, D., Tanaka, Y. A., & Vidotto, A. A. 2016, A&A, 591, A121
Brown, T. M. 2001, ApJ, 553, 1006
Chubb, K. L., Robert, S., Sousa-Silva, C., et al. 2024, RAS Tech. Instrum., 3, 636
Corless, R. M., Gonnet, G. H., Hare, D. E. G., Jeffrey, D. J., & Knuth, D. E. 1996, Adv. Computat. Math., 5, 329
de Wit, J., & Seager, S. 2013, Science, 342, 1473
Dos Santos, L. A., Vidotto, A. A., Vissapragada, S., et al. 2022, A&A, 659, A62
Espinoza, N., Steinrueck, M. E., Kirk, J., et al. 2024, Nature, 632, 1017
Gkouvelis, L. 2026, ApJ, 997, 307
Gkouvelis, L., Gérard, J.-C., Ritter, B., et al. 2018, J. Geophys. Res. (Planets), 123, 3119
Gkouvelis, L., Akın, C., & Heng, K. 2024, A&A, 690, A319
Gkouvelis, L., Pozuelos, F. J., Drant, T., et al. 2025, A&A, 699, A378
Heays, A. N., Bosman, A. D., & van Dishoeck, E. F. 2017, A&A, 602, A105
Koskinen, T. T., Yelle, R. V., Lavvas, P., & Lewis, N. K. 2010, ApJ, 723, 116
Koskinen, T. T., Harris, M. J., Yelle, R. V., & Lavvas, P. 2013, Icarus, 226, 1678
Lamers, H. J. G. L. M., & Cassinelli, J. P. 1999, Introduction to Stellar Winds
Lampón, M., López-Puertas, M., Sanz-Forcada, J., et al. 2023, A&A, 673, A140
Lecavelier Des Etangs, A., Pont, F., Vidal-Madjar, A., & Sing, D. 2008, A&A, 481, L83
Linssen, D. C., & Oklopčić, A. 2023, A&A, 675, A193
Linssen, D. C., Oklopčić, A., & MacLeod, M. 2022, A&A, 667, A54
Murray-Clay, R. A., Chiang, E. I., & Murray, N. 2009, ApJ, 693, 23
Oklopčić, A. & Hirata, C. M. 2018, ApJ, 855, L11
Owen, J. E. 2019, Annu. Rev. Earth Planet. Sci., 47, 67
Owen, J. E., Murray-Clay, R. A., Schreyer, E., et al. 2023, MNRAS, 518, 4357
Parker, E. N. 1958, ApJ, 128, 664
Seager, S., & Sasselov, D. D. 2000, ApJ, 537, 916
Steinrueck, M. E., Savel, A. B., Christie, D. A., et al. 2025, arXiv e-prints [arXiv:2509.21588]
Vidal-Madjar, A., Lecavelier des Etangs, A., Désert, J.-M., et al. 2003, Nature, 422, 143
Vidal-Madjar, A., Désert, J.-M., Lecavelier des Etangs, A., et al. 2004, ApJ, 604, L69
Watson, A. J., Donahue, T. M., & Walker, J. C. G. 1981, Icarus, 48, 150

Appendix A: Numerical transmission model

Fully numerical transmission spectra are computed using the Parker-wind density and velocity profiles. The atmospheric structure was described by a spherically symmetric, isothermal hydrodynamic outflow, for which the radial velocity $v(r)$ and number density $n(r)$ were obtained from the exact Parker solution. The profiles were computed from the planetary radius R_p up to $r_\mathrm{max} = 10\,R_\mathrm{p}$ and were used directly in the radiative transfer calculation.

The wavelength-dependent extinction cross section of the atmosphere was constructed as a volume–mixing–ratio–weighted sum of the individual species cross sections,

$$\sigma_\mathrm{mix}(\lambda) = \sum_i x_i\,\sigma_i(\lambda), \tag{A.1}$$

where x_i denotes the volume mixing ratio of species i. The same mixing ratios as in the analytical models were adopted.

For a given wavelength λ, the chord optical depth at impact parameter b was computed as

$$\tau_\lambda(b) = \int_{-\infty}^{+\infty} n(r(s))\ \sigma_\mathrm{mix}[\lambda'(s)]\ \mathrm{d}s, \tag{A.2}$$

where $r(s) = \sqrt{b^2 + s^2}$ is the radial distance along the line of sight. The Doppler-shifted wavelength $\lambda'(s)$ accounts for bulk hydrodynamic motion and is given by

$$\lambda'(s) = \lambda\left(1 - \frac{v_\mathrm{los}(s)}{c}\right), \tag{A.3}$$

with c the speed of light and $v_\mathrm{los}(s) = v(r)\,s/r$ the line-of-sight component of the radial wind velocity. This treatment naturally produces Doppler broadening due to the velocity gradient along the chord, as different regions of the atmosphere contribute at different projected velocities.

Thermal Doppler broadening was included by convolving the mixed cross section $\sigma_\mathrm{mix}(\lambda)$ with a Gaussian kernel in $\ln\lambda$, corresponding to a Maxwellian velocity distribution at the atmospheric temperature T_0. The fractional width of the kernel is $\sigma_{\ln\lambda} = v_\mathrm{th}/c$, where $v_\mathrm{th} = \sqrt{2k_\mathrm{B}T_0/m}$ is the thermal velocity of the absorbing species of mass m.

The wavelength-dependent transit depth was then obtained by integrating over all impact parameters,

$$\delta(\lambda) = \frac{1}{R_\star^2}\left[R_\mathrm{p}^2 + 2\int_{R_\mathrm{p}}^{b_\mathrm{max}} \left(1 - e^{-\tau_\lambda(b)}\right) b\,\mathrm{d}b\right], \tag{A.4}$$

where $R_\star$ is the stellar radius and b_max was chosen sufficiently large to enclose the optically thin upper atmosphere.

For resonance lines such as Lyα, the numerical spectra were computed on a high-resolution wavelength grid ($\Delta\lambda \lesssim 10^{-3}$ nm) in order to properly resolve both thermal and bulk Doppler broadening. At coarser wavelength resolution, the impact of velocity broadening on the integrated transit depth is reduced, particularly for optically thick lines.